Research Square

Preprints are preliminary reports that have not undergone peer review.
They should not be considered conclusive, used to inform clinical practice,
or referenced by the media as validated information.

Nanoscale Tire Wear Particles Disrupt the Blood–Testis Barrier and Impair Spermatogenesis through Oxidative Stress–Driven Ferritinophagy and Ferroptosis

Wenyang Pang
First Hospital of Jilin University
Yin Cao
First Hospital of Jilin University
Shuang Du
Affiliated Hospital of North Sichuan Medical College
Zuowen Liang
First Hospital of Jilin University
Hongliang Wang
First Hospital of Jilin University
Lingyun Liu
tmxlly@jlu.edu.cn

First Hospital of Jilin University

Research Article

Keywords: tire wear particles, blood-testis barrier, spermatogenesis, ferroptosis, ferritinophagy, oxidative stress

Posted Date: July 13th, 2026

DOI: https://doi.org/10.21203/rs.3.rs-10107696/v1

License: This work is licensed under a Creative Commons Attribution 4.0 International License.
Read Full License

Additional Declarations: No competing interests reported.

Version of Record: A version of this preprint was published at Journal of Nanobiotechnology on September 26th, 2026. See the published version at https://doi.org/10.1186/s12951-026-05106-6.

Abstract

Background

Tire wear particles (TWPs) are a major source of micro- and nanoplastics. However, reports on nanoscale tire wear particles, especially regarding their potential hazards to the male reproductive system, remain scarce.

Results

Here, we examined whether nanoscale tire wear particles impair spermatogenesis and blood-testis barrier integrity through oxidative stress-linked ferroptotic injury. Using a 70-day oral exposure model in pubertal male mice and complementary GC-2 and TM4 cell models, we found that high-dose particle exposure reduced epididymal sperm density, increased sperm abnormalities, disrupted seminiferous epithelial organization, and increased BTB permeability. TWPs shifted metabolomic profiles toward lipid and iron dysregulation, suppressed SLC7A11/GPX4, increased ACSL4 and labile Fe^{2+}, and depleted junctional proteins. Ferrostatin-1 reduced lipid peroxidation, iron accumulation, cell death, and junctional protein loss, indicating a functional contribution of ferroptosis. Mechanistically, TWPs first induced total and mitochondrial reactive oxygen species and mitochondrial depolarization, which were restrained by N-acetylcysteine. Downstream, autophagic ferritin degradation amplified ferroptotic injury, as chloroquine or NCOA4 knockdown preserved ferritin, reduced malondialdehyde accumulation, restored GPX4/SLC7A11, and improved viability. NCOA4 depletion did not substantially blunt ROS induction, placing ferritinophagy after oxidative stress.

Conclusions

Together, these data define a ROS-initiated, NCOA4-dependent ferritinophagy-ferroptosis axis that connects nanoscale TWPs to BTB failure and impaired spermatogenic homeostasis. This work provides a mechanistic basis for future assessment of reproductive health risks associated with TWPs exposure.

1. INTRODUCTION

Microplastics, a term introduced in 2004[1], have since been reported in air, freshwater and marine environments, and terrestrial soils. Atmospheric deposition, hydrological transport, and trophic transfer enable microplastics to move between environmental compartments and enter biological systems[2]. In recent years, their presence has been documented in plants, animals, and human tissues and biofluids[3–5]. These observations have raised concerns that sustained exposure to microplastics may adversely affect organismal health[6].

Among environmental microplastics, tire wear particles (TWPs) are produced in especially large quantities but remain comparatively underexplored [7]. They are produced as tires abrade against road surfaces during vehicle operation, releasing heterogeneous particles that span the micro- to nanoscale

range. The nanoscale tire wear particles warrants particular attention because its small dimensions, large specific surface area, and enhanced biological penetrability may facilitate their translocation across biological barriers, promote tissue accumulation, and trigger adverse responses such as oxidative stress, inflammation, and apoptosis[8–10].

Current toxicological research on TWPs remains limited and unevenly distributed across species and biological systems[11]. Most studies have focused on acute toxicity in aquatic organisms, alterations in soil microbial communities and tissue injury in terrestrial invertebrates[12]. In zebrafish, particle size appears to shape the toxicological response, with smaller TWPs associated with oxidative stress and larger particles with pronounced lipid metabolic disruption[13]. Photoaged TWPs impair antioxidant defence in earthworms, and high-dose exposure can produce oxidative stress and growth inhibition in rice seedlings[14, 15]. Although studies in mammalian models have gradually emerged, the available evidence remains scarce. Recent mouse studies indicate that TWPs exposure can disrupt the gut microbiota, induce hepatic injury[16], and elicit pulmonary inflammation and fibrosis[17]. Thus, TWPs may have systemic effects beyond their initial exposure route, but their impact on male reproductive function remains poorly defined.

Normal spermatogenesis depends on the ordered partnership between germ cells and Sertoli cells in the seminiferous epithelium[18]. This partnership is protected by the blood-testis barrier (BTB), a junctional structure formed mainly by adjacent Sertoli cells. The BTB supports germ-cell meiosis and maturation while separating developing germ cells from immune surveillance and circulating toxicants[19]. Barrier failure disrupts germ-cell positioning, interferes with meiotic progression, and reduces sperm output. Germ cells are also highly susceptible to oxidative injury because they have active metabolism, lipid-rich membranes, and strong dependence on mitochondrial function. Environmental toxicants that disturb redox balance, damage mitochondria, or weaken Sertoli-cell junctions may therefore compromise both BTB integrity and spermatogenesis[20].

Ferroptosis provides a plausible injury route in this setting. This regulated form of cell death depends on iron and lipid peroxide accumulation and is closely tied to glutathione depletion, mitochondrial dysfunction, and disordered iron handling[21]. Particulate pollutants have already been linked to ferroptotic tissue injury in several models[22–24]. Ferritinophagy may intensify this process: NCOA4 directs ferritin to autophagic degradation, releasing labile iron that can feed lipid peroxidation[25]. Disturbed iron handling and excessive oxidative stress have also been associated with testicular injury and BTB dysfunction[26,27]. Whether TWPs activate ferritinophagy-mediated ferroptosis and thereby impair the BTB and spermatogenesis has not been resolved.

To address this question, we combined a 70-day oral exposure model in pubertal male mice with GC-2 and TM4 cell experiments. Histopathology, BTB tracer assays, untargeted metabolomics, and rescue approaches with Ferrostatin-1 (Fer-1), N-acetylcysteine (NAC), chloroquine (CQ), and NCOA4 knockdown were used to map the injury sequence. The experiments were designed to test whether oxidative stress,

ferritinophagy, and ferroptosis connect nanoscale TWPs exposure with BTB disruption and impaired spermatogenesis.

2. MATERIALS AND METHODS

2.1. Preparation and Characterization of Tire Wear Particles. The preparation protocol for nanoscale tire wear particles was modified from previously reported methods[13, 47]. The raw tire wear particle material used in this study was supplied by Dujiangyan Huayi Rubber Co., Ltd. The company mechanically crushes end-of-life tires and preliminarily fractionates the resulting particles using sieves with different mesh sizes. The sieved particles were selected as the starting material and further processed to obtain TWPs through ethanol washing, ultrapure water rinsing, drying, cryogenic grinding, ball milling, ultrasonic dispersion, and differential centrifugation. The obtained TWPs were repeatedly washed and dried, then stored in sealed amber glass bottles at − 20°C until use. To minimize potential interference and particle aggregation, all TWPs working suspensions were freshly prepared on the day of each experiment and were vortexed and sonicated immediately before use. The detailed preparation procedure is provided in Supplementary Methods S1.

Morphology and size were assessed by SEM, TEM, and DLS, and surface charge was measured by zeta-potential analysis. FT-IR was used to examine surface functional groups, whereas EDS was used to determine elemental composition.

To trace the cellular uptake of TWPs, the particles were fluorescently labeled with Nile Red[48]. After labeling, the particles were thoroughly washed to remove unbound dye and were stored temporarily at 4°C in the dark. The detailed labeling protocol is provided in Supplementary Methods S2.

2.2. Animal Exposure and Experimental Design. Male BALB/c mice, 3 weeks of age, were purchased from Vital River Laboratory (Beijing, China). Animals were housed under specific pathogen-free conditions with a 12 h light/dark cycle, temperature of 22 ± 2°C, and relative humidity of 50 ± 10%. Food and water were available ad libitum. All procedures were approved by the Ethical Committee of the First Hospital of Jilin University (Approval No. JDYY20240270) and followed applicable guidelines for laboratory animal care.

After acclimatization, mice were assigned randomly to control, L-TWPs, or H-TWPs groups (n = 8 per group). TWPs were suspended in ultrapure water immediately before gavage and dispersed by vortexing plus sonication. Mice received daily oral gavage for 70 consecutive days. The doses were selected from earlier mouse gavage studies and preliminary tolerance observations: 5 mg kg^{-1} day^{-1} for L-TWPs and 50 mg kg^{-1} day^{-1} for H-TWPs. Control animals received the same volume of ultrapure water. The 70-day exposure window covered pubertal development and at least one complete spermatogenic cycle. Body weight and general health were monitored throughout.

For rescue experiments in vivo, mice were distributed into six groups (n = 8 per group): control, H-TWPs, H-TWPs plus Fer-1, H-TWPs plus NAC, Fer-1 alone, and NAC alone. TWPs-exposed groups received 50

mg kg^{-1} day^{-1} by oral gavage for 70 days. Fer-1 was given intraperitoneally at 2 mg kg^{-1} day^{-1}, and NAC was given intraperitoneally at 100 mg kg^{-1} day^{-1}. Single-agent groups followed the corresponding Fer-1 or NAC schedules.

Samples were collected 24 h after the final administration. Mice were euthanized under deep isoflurane anaesthesia, after which testes and epididymides were removed and weighed. Organ indices were calculated as organ weight/final body weight × 100%. Cauda epididymides were used for sperm concentration and morphology. One testis was fixed in 4% paraformaldehyde for histology, immunofluorescence, and BTB permeability testing; the contralateral testis was snap-frozen in liquid nitrogen and stored at − 80°C for protein and biochemical assays.

2.3. Sperm Parameter Analysis. Immediately after euthanasia, both cauda epididymides were placed in 1 mL PBS prewarmed to 37°C. The tissue was minced with ophthalmic scissors and incubated for 10–15 min at 37°C so that spermatozoa could swim out. After gentle mixing, 10 μL suspension was loaded into a haemocytometer for sperm counting under a light microscope. For morphology, aliquots were smeared on slides, air-dried, methanol-fixed, and eosin-stained. At least 200 spermatozoa were scored per animal. Normal and abnormal cells were counted, and abnormalities were grouped mainly as head, midpiece, or tail defects.

2.4. Testicular and Epididymal Indices. Body weight was measured before euthanasia. Testes and epididymides were dissected from both sides, cleared of adherent fat and connective tissue, and weighed. Indices were calculated by dividing testis or epididymis weight by body weight.

2.5. Histopathological Analysis. Testicular and epididymal tissues were fixed in 4% paraformaldehyde for 24 h. Samples were dehydrated through graded ethanol, paraffin-embedded, and cut into 5 μm sections. After deparaffinization and rehydration, sections were stained with H&E and examined under a light microscope. Testicular evaluation focused on seminiferous tubule structure, epithelial integrity, germ-cell arrangement, and sperm formation in the lumen. Epididymal evaluation focused on luminal sperm density, epithelial condition, and exfoliated cells.

2.6. Blood-Testis Barrier Permeability Assay. BTB permeability was tested with a biotin tracer. Under anaesthesia, testes were exposed, and EZ-Link Sulfo-NHS-LC-Biotin (Thermo Scientific, USA) was injected into the interstitial space beneath the tunica albuginea. The tracer was prepared at 10 mg/mL in PBS containing 1 mM $CaCl_2$, and 30 μL was delivered to each testis. The incision was sutured, and diffusion proceeded in vivo for 30 min before euthanasia and testis collection. Collected testes were embedded in OCT compound (Solarbio, China), snap-frozen, and sectioned at 5 μm. Cryosections were fixed for 20 min in 4% paraformaldehyde, washed with PBS, and blocked for 1 h in 5% BSA (Beyotime, China). FITC-conjugated streptavidin (Bioss, China) was applied for 1 h at room temperature in the dark. Nuclei were counterstained with DAPI (Beyotime, China), and sections were mounted with antifade medium before fluorescence imaging.

2.7. Cell Culture and Treatments. GC-2 (ATCC, CRL-2196) and TM4 (ATCC, CRL-1715) cells were obtained from the American Type Culture Collection. GC-2 cells were maintained in high-glucose DMEM (Gibco, USA) supplemented with 10% fetal bovine serum (Gibco, USA) and 1% penicillin-streptomycin

(Beyotime, China). TM4 cells were maintained in DMEM/F12 (Gibco, USA) with 5% horse serum (Procell, China), 2.5% fetal bovine serum, and 1% penicillin-streptomycin. Cells were cultured at 37°C in humidified 5% CO_2.

TWPs suspensions were prepared fresh for each experiment. Before treatment, suspensions were sonicated for 30 min in an ice bath. Cells at approximately 70–80% confluence were exposed for 24 h to 0, 12.5, 25, 50, 100, 200, 400, or 800 μg/mL TWPs. Mechanistic experiments used 400 μg/mL for 24 h unless otherwise stated (Figure S7A).

For pharmacological intervention, cells were pretreated with Fer-1 (1 μM), NAC (5 mM), or CQ (5 μM). TWPs were then added for 24 h, and samples were collected for the planned assays.

2.8. Cell Viability Assay. Viability was measured with CCK-8 reagent (Sparkjade, China). Cells were plated in 96-well plates and then treated as indicated. At the end of treatment, CCK-8 reagent was added for 1 h at 37°C. Absorbance was measured at 450 nm.

2.9. Live/Dead Cell Staining. Cell survival was assessed with Calcein-AM/propidium iodide staining (Beyotime, China). Treated cells were washed with PBS, incubated with the dye mixture for 20–30 min at 37°C in the dark, washed again, and imaged by fluorescence microscopy. Green signal indicated viable cells; red signal indicated membrane-compromised or dead cells.

2.10. Intracellular ROS Detection. Total intracellular ROS was detected with DCFH-DA. Cells were incubated with the probe for 20 min at 37°C protected from light, washed three times with PBS, and imaged by fluorescence microscopy.

2.11. Cellular Uptake and Cytoskeletal Staining. GC-2 and TM4 cells were treated for 24 h with Nile Red-labelled nanoscale TWPs to examine uptake and cytoskeletal organization. After exposure, cells were washed thoroughly, fixed with 4% paraformaldehyde, stained with phalloidin (Beyotime, China) for F-actin, and counterstained with DAPI. Fluorescence microscopy was used to evaluate intracellular TWPs localization and F-actin structure.

2.12. MDA Measurement. MDA in cells or testicular tissue was measured according to the kit protocol. Samples were lysed or homogenized, and supernatants were mixed with thiobarbituric acid working solution. The mixture was heated in boiling water for 60 min, cooled, and centrifuged at 3000 rpm for 10 min. Absorbance of the supernatant was read at 532 nm, and MDA was normalized to protein concentration.

2.13. Lipid Peroxidation Assay. Lipid peroxidation was assessed with C11-BODIPY 581/591. After 24 h TWPs exposure, GC-2 and TM4 cells were incubated with working solution for 15–30 min at 37°C in the dark. Cells were washed and imaged immediately.

2.14. FerroOrange Staining and Fe^{2+} Quantification. Labile Fe^{2+} was visualized with FerroOrange. Treated cells were incubated with 1 μM probe for 30 min at 37°C in the dark, washed, and imaged. Fe^{2+} in cells and testicular tissue was also quantified with a commercial iron assay kit according to the manufacturer's protocol and normalized to protein concentration.

2.15. Detection of Mitochondrial ROS and Mitochondrial Morphology. Mitochondrial structure and superoxide generation were examined with MitoTracker Green and MitoSOX Red. After 24 h TWPs exposure, cells were washed, stained with MitoTracker Green for 30 min at 37°C, and then incubated with MitoSOX Red for 10 min under light-protected conditions. Hoechst was used for nuclear counterstaining. MitoTracker Green was used to evaluate mitochondrial network morphology, and MitoSOX Red was used to detect mitochondrial ROS.

2.16. Assessment of Mitochondrial Membrane Potential. Mitochondrial membrane potential was measured with JC-1. Cells were incubated with JC-1 working solution for 20 min at 37°C in the dark, washed, and imaged.

2.17. NCOA4 siRNA Transfection. NCOA4 was knocked down with small interfering RNA. GC-2 and TM4 cells were seeded in six-well plates and transfected with si-NCOA4 or si-NC using TheriboFECT CP Transfection Kit (RiboBio, China). After 48 h, knockdown efficiency was checked by Western blotting (Figure S7C-D). Cells were then exposed to TWPs and collected for downstream experiments. Supplementary Table S1 lists the siRNA sequences.

2.18. Immunofluorescence Staining of Cells and Testicular Tissue. For cell staining, GC-2 and TM4 cells were grown on sterile coverslips in 12-well plates. After treatment, cells were washed, fixed in 4% paraformaldehyde for 15 min, and permeabilized with 0.5% Triton X-100 for 10 min. Paraffin-embedded testes were sectioned at 5 μm, deparaffinized, rehydrated, and subjected to antigen retrieval. Cells and tissue sections were blocked in 5% BSA for 1 h and incubated overnight at 4°C with primary antibodies. Antibody sources, catalogue numbers, and dilutions are provided in Supplementary Table S2.

The following day, samples were washed three times with PBS for 5 min each and incubated with fluorescent secondary antibodies for 1 h at room temperature in the dark. DAPI was used for nuclear counterstaining, and samples were mounted with antifade medium before imaging.

2.19. Western Blot Analysis. Total protein was extracted from mouse testes, GC-2 cells, and TM4 cells using ice-cold RIPA buffer containing PMSF and protease inhibitors. Cell lysates were prepared on ice after PBS washing. Testicular tissue was homogenized in lysis buffer. After centrifugation at 4°C, supernatants were collected, and protein concentration was measured with a BCA assay. Equal protein amounts were mixed with loading buffer, denatured, separated by SDS-PAGE, and transferred to PVDF membranes. Membranes were blocked for 1 h at room temperature and incubated overnight at 4°C with primary antibodies against ferroptosis, iron-homeostasis, ferritinophagy, and cell-function targets. β-actin or tubulin served as the loading control. Supplementary Table S2 provides antibody details.

Membranes were then washed with TBST and incubated for 1 h at room temperature with HRP-conjugated anti-rabbit or anti-mouse secondary antibodies. After washing, bands were developed with enhanced chemiluminescence reagent and recorded on a chemiluminescence imaging system.

2.20. Untargeted Metabolomics Analysis. GC-2 and TM4 cells subjected to control or TWPs exposure were collected for LC–MS-based untargeted metabolomics analysis, which was conducted by Lianchuan Bio. Briefly, intracellular metabolites were extracted using a precooled methanol/acetonitrile-based solvent system and reconstituted according to protein content to ensure normalized metabolite loading. Equal aliquots from each sample were pooled to generate quality-control (QC) samples, which were used to monitor analytical stability and reproducibility throughout the analytical sequence. Metabolomic profiling was performed on a Thermo Vanquish Flex UPLC system coupled to a Thermo Orbitrap Exploris 120 mass spectrometer, with data acquired in both positive and negative electrospray ionization modes. Raw data were processed for peak extraction, peak alignment, missing-value processing, normalization, and metabolite annotation. Differentially abundant metabolites were identified according to predefined statistical criteria and subsequently subjected to KEGG pathway enrichment analysis. Detailed procedures for sample preparation, chromatographic separation, mass spectrometric acquisition, and data processing are provided in Supplementary Method S3.

2.21. Transmission Electron Microscopy. TEM was used to examine cellular ultrastructure after TWPs exposure. Treated GC-2 and TM4 cells were collected, centrifuged into pellets, and fixed for 24 h at 4°C in 2.5% glutaraldehyde prepared in 0.1 M phosphate buffer. Pellets were rinsed, post-fixed in 1% osmium tetroxide for 3 h, dehydrated through graded ethanol, and embedded in epoxy resin. Ultrathin sections of about 60 nm were cut with an ultramicrotome and mounted on copper grids. After uranyl acetate and lead citrate staining, representative fields were examined by TEM.

2.22. Statistical Analysis. Statistical analyses were conducted in SPSS 25.0 (IBM, USA), and figures were prepared in GraphPad Prism 9.0 (GraphPad Software, La Jolla, CA, USA). Data are shown as mean ± SD from at least three independent experiments unless otherwise noted. Normality was tested with Shapiro-Wilk, and variance homogeneity with Levene's test. Two-group comparisons used a two-tailed unpaired Student's t-test. Multiple-group comparisons used one-way ANOVA followed by Tukey's post hoc test for homogeneous variances or Dunnett's T3 test for unequal variances. $P < 0.05$ was considered statistically significant.

3. RESULTS

3.1. Morphological and Physicochemical Characterization of TWPs. SEM and TEM showed that the prepared TWPs were irregular, nonspherical particles with rough surfaces and angular edges (Figure S1A,B), rather than the smooth polymer spheres often used as simplified micro- and nanoplastic models. DLS measured a hydrodynamic diameter of 125 ± 87 nm (Figure S1C), and zeta-potential analysis gave a surface potential of − 20.19 ± 6.53 mV (Figure S1F). FTIR spectroscopy was then used to examine surface chemistry (Figure S1D). The broad signal centred at 3279.34 cm^{-1} was assigned to O-H stretching, including surface hydroxyl groups or adsorbed water, whereas the band at 2922.30 cm^{-1} corresponded to aliphatic C-H stretching. Peaks at 1634.28, 1434.77, and 999.44 cm^{-1} were consistent with unsaturated rubber-related structures and hydrocarbon backbone vibrations. EDS detected dominant C and O signals together with Zn, Fe, and Ca (Figure S1E).

3.2. Exposure to TWPs Impairs Spermatogenesis and Disrupts Blood-Testis Barrier Integrity. To assess reproductive effects in vivo, 3-week-old male BALB/c mice were assigned to control, low-dose TWPs (L-TWPs; 5 mg kg^{-1} day^{-1}), or high-dose TWPs (H-TWPs; 50 mg kg^{-1} day^{-1}) groups and treated by oral gavage for 70 days. H-TWPs slowed body-weight gain during the later part of the exposure period (Fig. 1A). Testis and epididymis weights showed downward trends, but absolute organ weights and body weight-normalized indices did not differ significantly among groups (Fig. 1B-E).

Sperm evaluation showed that H-TWPs significantly lowered sperm density while increasing the frequency of abnormal spermatozoa (Fig. 1F,G). Histological sections revealed disordered seminiferous tubules, a thinner seminiferous epithelium, and reduced mature spermatozoa within the lumina of some tubules (Fig. 1H). The epididymal lumina likewise contained fewer spermatozoa and more cellular debris. In line with these tissue changes, DDX4 immunofluorescence was markedly reduced and was largely restricted to the basal region of the seminiferous tubules (Fig. 1I,L).

Given that continuous spermatogenesis requires an intact BTB, we next examined BTB organization and permeability. ZO-1 formed a continuous basal pattern along seminiferous tubules in control testes, whereas H-TWPs weakened and fragmented this signal (Fig. 1J,M). The biotin tracer was mostly confined to the basal compartment in control and L-TWPs mice. After H-TWPs exposure, however, biotin penetrated into the adluminal compartment, indicating barrier leakage (Fig. 1K). Immunoblotting confirmed reduced testicular levels of ZO-1, N-cadherin, occludin, and DDX4 in the H-TWPs group (Fig. 1N-R). Thus, high-dose oral TWPs exposure impaired sperm production and BTB integrity before significant changes in reproductive organ weight were evident.

3.3. Untargeted Metabolomics Links TWPs Exposure to Ferroptosis. Although in vivo observations indicated male reproductive toxicity after TWPs exposure, the cellular injury programme remained unclear. We therefore performed untargeted metabolomic profiling in GC-2 and TM4 cells treated with 400 μg/mL TWPs for 24 h. In GC-2 cells, 295 metabolites changed significantly, with 166 increased and 129 decreased metabolites (Fig. 2A). In TM4 cells, 297 metabolites were differentially abundant, including 186 increased and 111 decreased metabolites (Fig. 2B).

KEGG enrichment placed ferroptosis among the significantly affected pathways in both cell types. Lipid-associated pathways were also altered, including arachidonic acid metabolism in GC-2 cells and linoleic acid metabolism in TM4 cells. Gap-junction signalling was enriched in GC-2 cells as well. These patterns suggested that ferroptosis-related metabolic stress and impaired intercellular communication may contribute to TWPs-induced testicular toxicity.

We then asked whether the metabolic shifts were accompanied by changes in ferroptosis-associated proteins. TWPs exposure increased NCOA4 and ACSL4 while reducing ferritin, GPX4, and SLC7A11 in both cell lines (Fig. 2C,D and Figure S2A,B,E,F). Testes from H-TWPs-exposed mice showed a comparable protein signature (Fig. 2H and Figure S2I,J). Junctional proteins, including ZO-1, N-cadherin, and occludin, were also reduced in TWPs-treated GC-2 and TM4 cells (Fig. 2G,I and Figure S2C,G), mirroring the BTB-associated protein loss observed in vivo. Together, the metabolomic and protein data

indicate that TWPs provoke a ferroptosis-associated stress state while disrupting junctional homeostasis in testicular cells.

We further analysed F-actin because cytoskeletal organization is required for normal cell morphology and function. Control GC-2 and TM4 cells displayed regular morphology and well-arranged filamentous networks. After TWPs exposure, F-actin became disorganized and filament integrity was reduced (Fig. 2F). TWPs fluorescence was also detected inside cell boundaries. Calcein-AM/PI staining showed a lower green-to-red fluorescence ratio after exposure, consistent with reduced viability and increased cell death (Fig. 2E and Figure S2D,H). These observations confirmed direct cytotoxicity in both cell models.

3.4. Ferrostatin-1 Attenuates TWPs-Induced Cytotoxicity and Junctional Disruption. To test whether ferroptosis contributes functionally to TWPs-induced cell injury, we used the ferroptosis inhibitor ferrostatin-1 (Fer-1). TWPs exposure reduced testicular cell viability and increased intracellular malondialdehyde (MDA) and labile Fe^{2+}. Fer-1 pretreatment partially rescued viability and reduced both MDA accumulation and labile Fe^{2+} overload (Fig. 3A-C). Fluorescence imaging showed strong lipid-peroxidation signals after TWPs exposure, and this response was markedly weakened by Fer-1. Fer-1 also lowered the TWPs-induced intracellular labile Fe^{2+} signal (Fig. 3F,G and Figure S3I,K,T,V). At the protein level, Fer-1 countered the TWPs-induced increase in ACSL4 and NCOA4 and restored SLC7A11, ferritin, and GPX4 abundance. It also lessened the loss of ZO-1, N-cadherin, and occludin (Fig. 3D,E and Figure S3A-H,L-S). Immunofluorescence further showed better preservation of continuous ZO-1-positive junctional structures after Fer-1 treatment (Fig. 3H and Figure S3J,U). These rescue data support a causal role for ferroptosis in TWPs-induced cytotoxicity and junctional disruption in testicular cells.

3.5. Oxidative Stress Promotes TWPs-Induced Ferroptosis in GC-2 and TM4 Cells. We next asked whether redox disturbance preceded the ferroptotic response. DCFH-DA staining showed a clear increase in intracellular ROS after TWPs exposure in GC-2 and TM4 cells. NAC pretreatment markedly reduced this fluorescence signal (Fig. 4A and Figure S4D,J). TWPs also increased HO-1 and NQO1 in both cell lines and in testes from high-dose-exposed mice (Fig. 4B,C and Figure S4A-C), indicating that the oxidative-stress response was present in vitro and in vivo.

We then assessed mitochondrial dysfunction as a likely amplifier of oxidative injury. MitoSOX staining detected increased mitochondrial superoxide after TWPs exposure. MitoTracker imaging showed that the mitochondrial network became disrupted and more fragmented in both cell lines (Fig. 4F and Figure S4F,L). JC-1 staining indicated membrane-potential loss, as shown by a higher green/red fluorescence ratio (Fig. 4I and Figure S4E,K). These mitochondrial readouts coincided with lower viability and higher MDA levels (Fig. 4G,H).

NAC pretreatment reduced TWPs-induced cytotoxicity and lowered both total intracellular ROS and mitochondrial superoxide accumulation (Fig. 4A,F,G and Figure S4D,F,J,L). NAC also maintained mitochondrial membrane potential and restrained MDA production (Fig. 4H,I and Figure S4E,K), indicating that antioxidant treatment effectively blunts TWPs-induced oxidative and mitochondrial injury.

Finally, we examined whether oxidative stress was required for downstream ferroptosis-related signalling. NAC opposed the TWPs-induced changes in ferroptosis-associated proteins and antioxidant defence proteins (Fig. 4D,E and Figure S4G,H,M,N). These data place oxidative stress upstream of TWPs-induced ferroptotic injury. By reducing ROS accumulation, NAC limits mitochondrial damage and ferroptosis-associated signalling, thereby protecting GC-2 and TM4 cells from TWPs toxicity.

3.6. TWPs activate autophagic flux and ferritin degradation in GC-2 and TM4 Cells. TEM revealed ultrastructural changes compatible with autophagy after TWPs exposure (Figure S7B). Because these changes occurred alongside NCOA4 induction and ferritin depletion, we asked whether NCOA4-dependent ferritinophagy contributes to ferroptotic injury. We reanalysed the untargeted metabolomic dataset with attention to autophagy- and ferroptosis-related metabolites. Hierarchical clustering showed increased abundance of several polyunsaturated fatty acids, including arachidonic acid, linoleic acid, and related metabolites, in both GC-2 and TM4 cells after exposure. These lipids can serve as substrates for peroxidation. In contrast, redox-associated metabolites such as glutathione and glutamine were depleted, indicating a metabolic environment favourable to ferroptosis. The autophagy-related polyamines spermine and spermidine were also altered, further suggesting engagement of autophagic pathways (Fig. 5A).

To test this possibility directly, we measured the canonical autophagy markers LC3B and p62. TWPs increased the LC3B-II/LC3B-I ratio and reduced p62 abundance in mouse testes, GC-2 cells, and TM4 cells (Fig. 5B and Figure S5J-L), a pattern consistent with increased autophagic activity. Immunofluorescence also showed greater colocalization between ferritin and LC3B-positive puncta after exposure, indicating recruitment of ferritin to autophagosomes (Fig. 5C). When considered with NCOA4 induction and ferritin loss, these results implicate ferritinophagy in the cellular response to TWPs.

We then used chloroquine (CQ), a late-stage autophagy inhibitor, to determine whether autophagic activity supports ferroptotic progression. CQ increased LC3B-II accumulation and restored p62, consistent with blocked autophagic turnover (Fig. 5D and Figure S5H,I,T,U). Autophagy blockade reduced the TWPs-induced ferroptosis protein signature: ferritin, SLC7A11, and GPX4 recovered, whereas ACSL4 declined (Fig. 5D and Figure S5A-D,M-O). In contrast, CQ had little effect on HO-1 or NQO1 induction and did not fully suppress NCOA4 accumulation (Fig. 5D and Figure S5E-G,P-S). Thus, late-stage autophagy inhibition mainly restrained ferritin degradation and downstream ferroptosis without eliminating the upstream oxidative-stress response.

Taken together, these results place oxidative stress before the ferroptotic cascade, while autophagy-dependent ferritin degradation supplies a downstream iron-mobilizing step that connects ROS accumulation to ferroptosis execution. Ferritinophagy therefore acts as an amplification mechanism in TWPs-induced ferroptotic injury.

3.7. NCOA4 Links TWPs-Induced Oxidative Stress to Ferritinophagy-Driven Ferroptotic Injury. To define the contribution of NCOA4-dependent ferritinophagy, we depleted NCOA4 in GC-2 and TM4 cells using small interfering RNA (Figure S7C,D). Even with efficient NCOA4 silencing, TWPs exposure produced

similar increases in DCFH-DA fluorescence in si-NCOA4- and si-NC-transfected cells (Fig. 6A-C). NCOA4 depletion also had little influence on HO-1 and NQO1 induction (Fig. 6F-I). These findings indicate that oxidative stress develops independently of NCOA4 and most likely precedes NCOA4-mediated ferritinophagy. In contrast, NCOA4 silencing significantly reduced TWPs-induced MDA accumulation and improved cell viability (Fig. 6D,E). Consistent with these effects, NCOA4 depletion maintained ferritin abundance and partially restored GPX4 and SLC7A11 expression (Fig. 6F-I). These results support a pathway in which NCOA4-dependent ferritinophagy translates TWPs-induced oxidative stress into ferritin loss and lipid peroxidation, thereby promoting ferroptotic injury.

3.8. Ferroptosis Blockade and Antioxidant Intervention Mitigate TWPs-Induced Testicular Injury In Vivo. To validate the contribution of ferroptosis and oxidative stress in vivo, we conducted rescue experiments using Fer-1 and the broad-spectrum antioxidant NAC. Compared with mice exposed to TWPs alone, both interventions reduced testicular Fe^{2+} accumulation and MDA production (Fig. 7C,D). Western blotting showed that Fer-1 and NAC also buffered the TWPs-induced disruption of protein expression. TWPs exposure reduced GPX4, SLC7A11, ferritin, DDX4, ZO-1, N-cadherin, and occludin, while increasing ACSL4, NCOA4, HO-1, and NQO1. These shifts were markedly weakened by Fer-1 or NAC treatment, supporting a close relationship among ferroptotic stress, redox imbalance, disrupted spermatogenic homeostasis, and BTB dysfunction after TWPs exposure (Fig. 7A).

The biotin tracer assay was consistent with the molecular data. TWPs caused clear BTB leakage, with biotin diffusing from the basal compartment into the adluminal region of seminiferous tubules. Fer-1 and NAC restricted this penetration, leaving most of the signal near the basal compartment. H&E staining further showed that TWPs disrupted seminiferous epithelial organization, weakened intercellular cohesion, and disturbed germ-cell arrangement. Both interventions alleviated these histopathological changes, as shown by better-preserved tubule architecture, more orderly spermatogenic epithelial stratification, and less structural injury (Fig. 7B).

Overall, the intervention experiments provide functional in vivo evidence that oxidative stress and ferroptosis are key mediators of TWPs-induced male reproductive toxicity. Ferroptosis inhibition and antioxidant treatment reduced iron overload and lipid peroxidation, restored major ferroptosis- and antioxidant-related protein signatures, protected BTB integrity, and mitigated testicular tissue damage. These findings reinforce the mechanistic link between TWPs exposure and the ROS-ferroptosis axis in the testis.

4. DISCUSSION

Tire wear particles constitute a large and still incompletely understood class of environmental microplastics. Road traffic, braking, and tire-road friction continuously generate particles across a broad size spectrum[28]. The nanoscale fraction is toxicologically important because a smaller size increases surface area, environmental mobility, and opportunities for contact with biological barriers. Tire-particle emissions have been estimated at approximately 0.81 kg per capita each year, corresponding to nearly

6.1 million tons globally[29]. TWPs have been detected in air, soil, and aquatic systems, and the available evidence indicates that they can become bioavailable to multiple organisms. Even so, toxicological research has centred largely on aquatic models, leaving mammalian in vivo evidence, especially for reproductive outcomes, relatively limited[30].

The male reproductive system is sensitive to environmental toxicants because testicular structure and spermatogenic progression depend on redox control, BTB integrity, and coordinated cellular metabolism[18–20]. In our in vivo model, subchronic TWPs exposure did not significantly change testis or epididymis coefficients, although the high-dose group showed modestly reduced body-weight gain. This pattern suggests that functional reproductive endpoints may respond before gross organ indices shift during subchronic environmental exposure. Indeed, high-dose TWPs reduced epididymal sperm density and increased morphologically abnormal sperm. These defects were accompanied by disordered seminiferous tubules, epithelial thinning, germ-cell exfoliation, and reduced DDX4, indicating impaired spermatogenesis. BTB disruption provides a structural explanation for this phenotype. The BTB maintains testicular immune privilege and protects developing germ cells, relying on tight-junction proteins such as ZO-1 and occludin and adherens-junction proteins such as N-cadherin[19]. Biotin tracing, immunofluorescence, and immunoblotting showed that TWPs weakened junctional-protein expression and continuity while increasing BTB permeability. Such barrier failure could permit particles or soluble toxic mediators to reach the adluminal compartment, thereby worsening germ-cell injury.

BTB damage is now recognized as one route by which environmental contaminants compromise male fertility[31–33]. In this study, GC-2 spermatocytes developed ferroptosis-related injury after TWPs exposure, indicating that germ cells are intrinsically vulnerable to particulate stress. TM4 Sertoli cells, in parallel, lost junction-associated proteins and showed weakened ferroptosis defence. These findings suggest a dual injury mode: TWPs directly damage germ cells while also destabilizing the Sertoli-cell barrier niche that supports spermatogenesis.

Ferroptosis offers a mechanistic connection among TWPs exposure, iron imbalance, lipid oxidation, and reproductive cell damage. This regulated death pathway is driven by iron-dependent lipid peroxidation and has been implicated in toxicant-induced injury in several organs, including the testis. Recent work has connected ferroptosis with testicular damage caused by environmental toxicants such as GLA and polystyrene microplastics[34, 35]. However, whether TWPs use a ferroptotic mechanism in reproductive toxicity, and how that mechanism begins, has remained uncertain. Our untargeted metabolomics showed that TWPs strongly altered the metabolic profiles of GC-2 and TM4 cells. Differential metabolites were enriched in ferroptosis-, lipid-metabolism-, and cell-junction-related pathways. Accumulation of polyunsaturated fatty acids, coupled with glutathione depletion, provided omics-level evidence that ferroptosis is a prominent molecular event in TWPs-induced testicular cell injury.

Protein and functional assays supported this interpretation. TWPs increased ACSL4, suppressed the SLC7A11/GPX4 antioxidant axis, elevated intracellular Fe^{2+}, and enhanced MDA accumulation. These changes appeared in both cell models and testicular tissue, suggesting that ferroptosis is shared across

the in vitro and in vivo systems. Fer-1 treatment restored cell viability, decreased lipid peroxidation, rescued key BTB-associated proteins, and reduced barrier-related injury. These rescue findings argue that ferroptotic activation is not merely associated with TWPs toxicity, but contributes to spermatogenic impairment and BTB disruption.

Oxidative stress appears to initiate the pathway leading to ferroptosis. Nanoparticle toxicity often begins with redox disturbance, mitochondrial stress, and reduced antioxidant capacity[36, 37]. Consistent with this framework, TWPs increased intracellular ROS, mitochondrial ROS, HO-1, and NQO1, while damaging mitochondrial morphology and reducing membrane potential. NAC lowered ROS, improved mitochondrial function, and prevented downstream ferroptosis-related activation. These results place oxidative stress at the upstream end of the TWPs-induced reproductive injury cascade.

Previous reports on TWPs-induced oxidative stress have not been uniform. Some macrophage studies did not find a marked ROS increase[38, 39], whereas studies in algae, fish, rotifers, sludge microorganisms, plants, or aged-TWPs systems reported oxidative damage, altered antioxidant-enzyme activity, or enhanced ROS generation[40–42]. These differences probably reflect variation in particle source, size distribution, weathering state, exposure conditions, and cell type. Nanoscale particles may interact more readily with membranes, protein coronas, and mitochondria. Metal-containing components can perturb metal homeostasis and antioxidant capacity, while environmental ageing can generate environmentally persistent free radicals (EPFRs) that support ROS formation. Studies of photoaged and black microplastics are consistent with a role for EPFRs and ageing-related chemistry in oxidative injury[43]. Because testicular cells are particularly sensitive to mitochondrial damage, lipid oxidation, and iron imbalance, negative ROS results in other models do not exclude the oxidative response observed here in reproductive cells and tissue.

Autophagy-dependent control of intracellular iron is increasingly recognized as an important regulator of ferroptosis. Ferritin stores intracellular iron and buffers the labile iron pool. NCOA4 acts as a selective cargo receptor that delivers ferritin to the autophagy-lysosome pathway for degradation, thereby releasing stored iron and expanding the redox-active Fe^{2+} pool. Previous studies have mainly addressed NCOA4-mediated ferritinophagy in cancer, lung injury, and selected nanoparticle exposure models[44–46]. Its role in male reproductive toxicity, especially after TWPs exposure, has received much less attention.

Our results show that TWPs increased NCOA4, reduced ferritin, enhanced ferritin-LC3B colocalization, increased LC3B-II/I, and decreased p62, indicating autophagic activation and recruitment of ferritin into degradative pathways. Chloroquine blockade restored ferritin, GPX4, and SLC7A11 and reduced ACSL4. NCOA4 knockdown more specifically maintained ferritin, lowered lipid peroxidation, improved viability, and restored GPX4/SLC7A11 expression. These data indicate that NCOA4-dependent ferritinophagy is not simply a parallel marker of ferroptosis, but a functional relay that converts oxidative stress into iron-dependent lipid peroxidation.

The intervention results also clarify pathway order. Chloroquine and NCOA4 knockdown did not strongly suppress ROS accumulation, but both reduced ferroptosis and junctional injury. NAC, by contrast, suppressed ROS and prevented downstream ferritinophagy-ferroptosis activation. This pattern supports a hierarchy in which TWPs first trigger oxidative stress and mitochondrial damage. NCOA4-dependent ferritinophagy then weakens ferritin-mediated iron buffering, enlarges the labile iron pool, and promotes lipid peroxidation. Ferroptosis subsequently drives injury in germ cells and Sertoli cells. In this model, oxidative stress is upstream, NCOA4-mediated ferritinophagy mobilizes iron, and ferroptosis executes the cellular injury programme.

Several limitations should be noted. First, the TWPs used here were prepared from tire-derived material and are more environmentally relevant than pristine commercial polymer beads, but they still cannot represent the full diversity of particles generated under road conditions. Tire formulation, pavement composition, brake-wear contamination, weathering, photoaging, and long-term environmental ageing can all change particle chemistry and toxicity. Second, this work focused on nanoscale TWPs, whereas environmental tire debris also contains micrometre-sized particles. Size-dependent differences in deposition, biodistribution, cellular uptake, and reproductive effects require further study. Third, EPFRs may contribute to ROS generation by aged or carbonaceous particles, but they were not directly measured here. Finally, the present study examined subchronic exposure and mechanistic injury endpoints. Transgenerational effects, fertility outcomes, and lifelong low-dose exposure remain unresolved. Because human exposure is likely chronic, mixed, and cumulative, the long-term reproductive implications of TWPs need continued investigation.

5. CONCLUSION

In summary, our findings show that nanoscale TWPs can impair male reproductive function by damaging the spermatogenic epithelium and disrupting the BTB. The data support a two-step injury model. First, reactive nanoscale composite particles interact with germ cells and Sertoli cells, causing total and mitochondrial ROS accumulation, mitochondrial membrane-potential loss, and redox imbalance. Second, sustained oxidative stress activates NCOA4-mediated ferritinophagy, reduces ferritin-dependent iron buffering, increases the labile iron pool, and promotes lipid peroxidation and ferroptotic execution. Ferroptosis then weakens Sertoli-cell junctions and germ-cell homeostasis, resulting in higher BTB permeability, reduced junctional proteins, lower DDX4 expression, decreased sperm density, and more abnormal spermatozoa. By linking nanoscale TWPs exposure to the oxidative stress-NCOA4 ferritinophagy-ferroptosis axis, this study provides mechanistic evidence for evaluating possible reproductive health risks associated with TWPs.

Abbreviations

ACSL4
acyl-CoA synthetase long-chain family member 4
BTB

blood-testis barrier
CCK-8
Cell Counting Kit-8
CQ
chloroquine
DAPI
4',6-diamidino-2-phenylindole
DCFH-DA
2',7'-dichlorodihydrofluorescein diacetate
DDX4
DEAD-box helicase 4
DLS
dynamic light scattering
EDS
energy-dispersive X-ray spectroscopy
Fer-1
Ferrostatin-1
FTIR
Fourier-transform infrared spectroscopy
GC-2
mouse spermatocyte cell line
GPX4
glutathione peroxidase 4
H&E
hematoxylin and eosin
LC-MS
liquid chromatography-mass spectrometry
MDA
malondialdehyde
NAC
N-acetylcysteine
NCOA4
nuclear receptor coactivator 4
ROS
reactive oxygen species
SEM
scanning electron microscopy
SLC7A11
solute carrier family 7 member 11
TEM

transmission electron microscopy
TM4
mouse Sertoli cell line
TWPs
tire wear particles
ZO-1
zonula occludens-1.

Declarations

Acknowledgements

We sincerely acknowledged the core facility of The First Hospital of Jilin University, for providing access to experimental equipment and testing facilities.

Author contributions

Wenyang Pang, Hongliang Wang, and Lingyun Liu conceived and designed the study. Wenyang Pang, Yin Cao and Zuowen Liang performed the experiments. Wenyang Pang, Shuang Du and Yin Cao analyzed the data and prepared the figures. Wenyang Pang drafted the manuscript. Hongliang Wang and Lingyun Liu supervised the project and revised the manuscript critically for important intellectual content. All authors read and approved the final manuscript.

Funding

The present study was supported by the Study of serum exosome miRNAs in the diagnosis of testicular cancer (2022GL011); the Project of Scientific Research Development Fund of North Sichuan Medical College (Grant CBY22-QNA58) and the Project of Scientific Research Development Fund of North Sichuan Medical College (Grant CBY23-QNA03).

Data availability

No datasets were generated or analyzed during the current study.

Ethics approval and consent to participate

All animal procedures were approved by the Ethical Committee of the First Hospital of Jilin University (Approval No. JDYY20240270) and were conducted in accordance with relevant institutional guidelines for laboratory animal care.

Consent for publication

Not applicable.

Competing interests

The authors declare no competing financial interest.

AUTHOR INFORMATION

Corresponding Authors

Lingyun Liu - Department of Andrology, The First Hospital of Jilin University, Changchun 130000, China. E-mail: tmxlly@jlu.edu.cn; orcid.org/0000-0002-6755-1259.

Hongliang Wang - Department of Andrology, The First Hospital of Jilin University, Changchun 130000, China. E-mail: hongliang@jlu.edu.cn; orcid.org/0000-0002-1941-3003.

Authors

Wenyang Pang - [1]Department of Andrology, The First Hospital of Jilin University, Changchun 130000, China; [2]Department of Urology, Affiliated Hospital of North Sichuan Medical College, Nanchong 637200, China. E-mail: pangwy23@mails.jlu.edu.cn;https://orcid.org/0000-0002-6853-7336.

Yin Cao - Department of Andrology, The First Hospital of Jilin University, Changchun 130000, China. E-mail: caoyin21@jlu.edu.cn; orcid.org/0000-0002-2321-7478.

Shuang Du - Department of Dermatology, Affiliated Hospital of North Sichuan Medical College, Nanchong, China. E-mail: dushuang0928@163.com; orcid.org/0009-0000-3976-708X.

Zuowen Liang - Department of Andrology, The First Hospital of Jilin University, Changchun 130000, China. E-mail: liangzw@jlu.edu.cn; orcid.org/0009-0002-2196-1882.

References

1. Thompson RC, Olsen Y, Mitchell RP, Davis A, Rowland SJ, John AW, et al. Lost at sea: where is all the plastic? Science. 2004;304(5672):838.
2. Allen S, Allen D, Phoenix VR, Le Roux G, Durántez Jiménez P, Simonneau A, et al. Atmospheric transport and deposition of microplastics in a remote mountain catchment. Nat Geosci. 2019;12(5):339–44.
3. Li R, Lin F, Zhao X, Wang J, Teng M, Li C, et al. Microplastics and nanoplastics in brain tumours and the healthy human brain. Nat Health. 2026;1(6):633–46.
4. Schwabl P, Köppel S, Königshofer P, Bucsics T, Trauner M, Reiberger T, et al. Detection of Various Microplastics in Human Stool: A Prospective Case Series. Ann Intern Med. 2019;171(7):453–7.
5. Leslie HA, van Velzen MJM, Brandsma SH, Vethaak AD, Garcia-Vallejo JJ, Lamoree MH. Discovery and quantification of plastic particle pollution in human blood. Environ Int. 2022;163:107199.

6. Cui C, Guo Z, Liu Y, Han N, Song J, Chen Y, et al. Tissue-specific distribution of microplastics in human blood and carotid plaques: A paired sample analysis. Environ Int. 2025;203:109743.
7. Liu Z, Wang G, Ye X, Zhang X, Jiang Y, Han Y, et al. Multigenerational toxic effects in Daphnia pulex are induced by environmental concentrations of tire wear particle leachate. J Hazard Mater. 2025;486:136977.
8. Jurkschat L, Gill AJ, Milner R, Holzinger R, Evangeliou N, Eckhardt S, et al. Using a citizen science approach to assess nanoplastics pollution in remote high-altitude glaciers. Sci Rep. 2025;15(1):1864.
9. Stenzel MH. The dark matter in water, air and land: from microplastic to invisible nanoplastics. Mater Horiz. 2026;13(4):1628–48.
10. Cunningham B, Harper B, Brander S, Harper S. Toxicity of micro and nano tire particles and leachate for model freshwater organisms. J Hazard Mater. 2022;429:128319.
11. Obanya HE, Khan FR, Carrasco-Navarro V, Rødland ES, Walker-Franklin I, Thomas J, et al. Priorities to inform research on tire particles and their chemical leachates: A collective perspective. Environ Res. 2024;263(Pt 3):120222.
12. Parker BW, Beckingham BA, Ingram BC, Ballenger JC, Weinstein JE, Sancho G. Microplastic and tire wear particle occurrence in fishes from an urban estuary: Influence of feeding characteristics on exposure risk. Mar Pollut Bull. 2020;160:111539.
13. Zhang Y, Song Q, Meng Q, Zhao T, Wang X, Meng X, et al. Size-dependent ecotoxicological impacts of tire wear particles on zebrafish physiology and gut microbiota: Implications for aquatic ecosystem health. J Hazard Mater. 2025;487:137215.
14. Chen L, Liu Z, Yang T, Zhao W, Yao Y, Liu P, et al. Photoaged Tire Wear Particles Leading to the Oxidative Damage on Earthworms (Eisenia fetida) by Disrupting the Antioxidant Defense System: The Definitive Role of Environmental Free Radicals. Environ Sci Technol. 2024;58(10):4500–9.
15. Wasnik S, Cheng S, Zhao X, Keang K, Zhang H, Cross JS. Tire wear particle and leachate induce oxidative stress and reshape the rice rhizosphere soil system: Multi-omics evidence of tissue-specific phytotoxicity. J Hazard Mater. 2026;513:142458.
16. Zhou Y, Cheng P, Ran J, Li X, Yan X, Luo L, et al. Integrated multi-omics of gut-liver axis to dissect the mechanism underlying hepatotoxicity induced by sub-chronic tire wear particles exposure in mice. Ecotoxicol Environ Saf. 2025;306:119350.
17. Li Y, Shi T, Li X, Sun H, Xia X, Ji X, et al. Inhaled tire-wear microplastic particles induced pulmonary fibrotic injury via epithelial cytoskeleton rearrangement. Environ Int. 2022;164:107257.
18. Wu S, Yan M, Ge R, Cheng CY. Crosstalk between Sertoli and Germ Cells in Male Fertility. Trends Mol Med. 2020;26(2):215–31.
19. Wang X, Jiang F, Yang H, Niu D, Xi H. Advances in understanding the dual roles of testicular immune responses: From immune privilege to inflammation. Semin Immunopathol. 2026;48(1).
20. Zhang L, Gao S, Xiong X, Liu X, Li R, Wang X, et al. Norepinephrine Induces Sertoli Cell Ferroptosis via Receptors Desensitization Causing Stress-Related Male Reproductive Dysfunction. Adv Sci

(Weinh). 2025;12(48):e04817.
21. Dixon SJ, Olzmann JA. The cell biology of ferroptosis. Nat Rev Mol Cell Biol. 2024;25(6):424–42.
22. Wei YY, Chen TT, Zhang DW, Zhang Y, Li F, Ding YC, et al. Microplastics exacerbate ferroptosis via mitochondrial reactive oxygen species-mediated autophagy in chronic obstructive pulmonary disease. Autophagy. 2025;21(8):1717–43.
23. Yang S, Zhang T, Ge Y, Cheng Y, Yin L, Pu Y, et al. Ferritinophagy Mediated by Oxidative Stress-Driven Mitochondrial Damage Is Involved in the Polystyrene Nanoparticles-Induced Ferroptosis of Lung Injury. ACS Nano. 2023;17(24):24988–5004.
24. Chen Z, Zheng M, Wan T, Li J, Yuan X, Qin L, et al. Gestational exposure to nanoplastics disrupts fetal development by promoting the placental aging via ferroptosis of syncytiotrophoblast. Environ Int. 2025;197:109361.
25. Hou W, Xie Y, Song X, Sun X, Lotze MT, Zeh HJ 3, et al. Autophagy promotes ferroptosis by degradation of ferritin. Autophagy. 2016;12(8):1425–8.
26. Zeng Y, Yang Q, Ouyang Y, Lou Y, Cui H, Deng H, et al. Nickel induces blood-testis barrier damage through ROS-mediated p38 MAPK pathways in mice. Redox Biol. 2023;67:102886.
27. Zhao Y, Zhang H, Cui JG, Wang JX, Chen MS, Wang HR, et al. Ferroptosis is critical for phthalates driving the blood-testis barrier dysfunction via targeting transferrin receptor. Redox Biol. 2023;59:102584.
28. Zeb A, Shi R, Liu W, Khan S, Baig AM, Iqbal H, et al. A critical review of tire wear particles aging and ecotoxicological consequences in terrestrial environments: Insights into environmentally persistent free radicals. J Hazard Mater. 2026;501:140641.
29. Breider F, Masset T, Prud'homme K, Brüschweiler BJ. Assessment of tire-derived additives and their metabolites into fruit, root and leafy vegetables and evaluation of dietary intake in Swiss adults. J Hazard Mater. 2025;494:138432.
30. Xu Q, Kazmi S, Li G. Tracking the biogeochemical behavior of tire wear particles in the environment - A review. J Hazard Mater. 2024;480:136184.
31. Zheng S, Zhao N, Lin X, Jiang L, Qiu C, Jiang J, et al. Fine Particulate Matter (PM2.5) and the Blood-Testis Barrier: An in Vivo and in Vitro Mechanistic Study. Environ Health Perspect. 2025;133(3–4):47006.
32. Zhao Q, Fang Z, Wang P, Qian Z, Yang Y, Ran L, et al. Polylactic Acid Micro/Nanoplastic Exposure Induces Male Reproductive Toxicity by Disrupting Spermatogenesis and Mitochondrial Dysfunction in Mice. ACS Nano. 2025;19(5):5589–603.
33. Zhang Y, Shu M, Shan S, Liu H, Zhang Y, Song C, et al. Perfluorohexane Sulfonic Acid Disrupts the Immune Microenvironment for Spermatogenesis by Damaging the Structure of the Blood-Testis Barrier in Mice. Adv Sci (Weinh). 2025;12(10):e2409383.
34. Wang D, Zhang C, Yang F, Hu Y, Xing C, Hu G et al. AMPK-ULK1-Mediated Ferritinophagy Drives Ferroptosis in GLA-Induced Testicular Toxicity. Research (Wash D C). 2025;8:0860.

35. Lv J, Liu G, Wang Z, Zhang J, Li Y, Wang Y, et al. Internalized polystyrene nanoplastics trigger testicular damage and promote ferroptosis via CISD1 downregulation in mouse spermatocyte. J Nanobiotechnol. 2025;23(1):537.
36. Xuan L, Ju Z, Skonieczna M, Zhou PK, Huang R. Nanoparticles-induced potential toxicity on human health: Applications, toxicity mechanisms, and evaluation models. MedComm (2020). 2023;4(4):e327.
37. He Y, Yu T, Li H, Sun Q, Chen M, Lin Y, et al. Polystyrene nanoplastic exposure actives ferroptosis by oxidative stress-induced lipid peroxidation in porcine oocytes during maturation. J Anim Sci Biotechnol. 2024;15(1):117.
38. Bouredji A, Muresan B, Truong XT, Lumière L, Pourchez J, Forest V. An in vitro comparison of the toxicological profiles of ground tire particles (TP) and actual tire and road wear particles (TRWP) emissions. Environ Int. 2024;190:108885.
39. Bouredji A, Lumière L, Lakhmi R, Muresan-Paslaru B, Pourchez J, Forest V. A toxicological comparison of tire and road wear particles emitted on rural and urban roads, alone or with the co-exposed pollutant benzo[a]pyrene: Size and origin as key factors in controlling the in vitro proinflammatory response. Environ Int. 2025;205:109920.
40. Liu Z, Sun Y, Wang J, Li J, Jia H. In Vitro Assessment Reveals the Effects of Environmentally Persistent Free Radicals on the Toxicity of Photoaged Tire Wear Particles. Environ Sci Technol. 2022;56(3):1664–74.
41. Xia W, Geng Z, Meng Z, Li Z, Lian F, Xing B. Photoaging-Driven Transformation of Tire Wear Particles: Unraveling the Spatiotemporal Dynamics of Persistent Free Radicals and Their Phytotoxic Impact. Environ Sci Technol. 2026;60(1):996–1006.
42. Chen X, Wu M, Cao X, Wang Z. Unveiling the toxic mechanism of nanoscale tire wear particles to algae: The interplay of particle size, photoaging, and co-existing PFOS. Water Res. 2026;296:125602.
43. Zhang P, Tang X, Qin N, Shuai Y, Wang J, Wang H, et al. Advanced understanding of the natural forces accelerating aging and release of black microplastics (tire wear particles) based on mechanism and toxicity analysis. Water Res. 2024;266:122409.
44. Zhao X, Kang Z, Han R, Wang M, Wang Y, Sun X, et al. JWA binding to NCOA4 alleviates degeneration in dopaminergic neurons through suppression of ferritinophagy in Parkinson's disease. Redox Biol. 2024;73:103190.
45. Santana-Codina N, Del Rey MQ, Kapner KS, Zhang H, Gikandi A, Malcolm C, et al. NCOA4-Mediated Ferritinophagy Is a Pancreatic Cancer Dependency via Maintenance of Iron Bioavailability for Iron-Sulfur Cluster Proteins. Cancer Discov. 2022;12(9):2180–97.
46. Huang X, Feng J, Xu Q, Tang R, Peng Y, Yang W, et al. NCOA4-Mediated Ferritinophagy Induces Ferroptosis and Enriches Ferritin-Containing EVs via Ferritin Phase Separation to Promote Mechanical Ventilation-Induced Pulmonary Fibrosis. J Adv Res. 2026;82:449–67.
47. Ji Y, Chen L, Wang Y, Zhang J, Yu Y, Wang M, et al. Realistic Nanoplastics Induced Pulmonary Damage via the Crosstalk of Ferritinophagy and Mitochondrial Dysfunction. ACS Nano.

2024;18(26):16790–807.

48. Lian H, Zhu L, Zha C, Li M, Feng S, Gao F, et al. Toxicity and intergenerational accumulation effect of tire wear particles and their leachate on Brachionus plicatilis. Environ Pollut. 2025;367:125635.

Figures

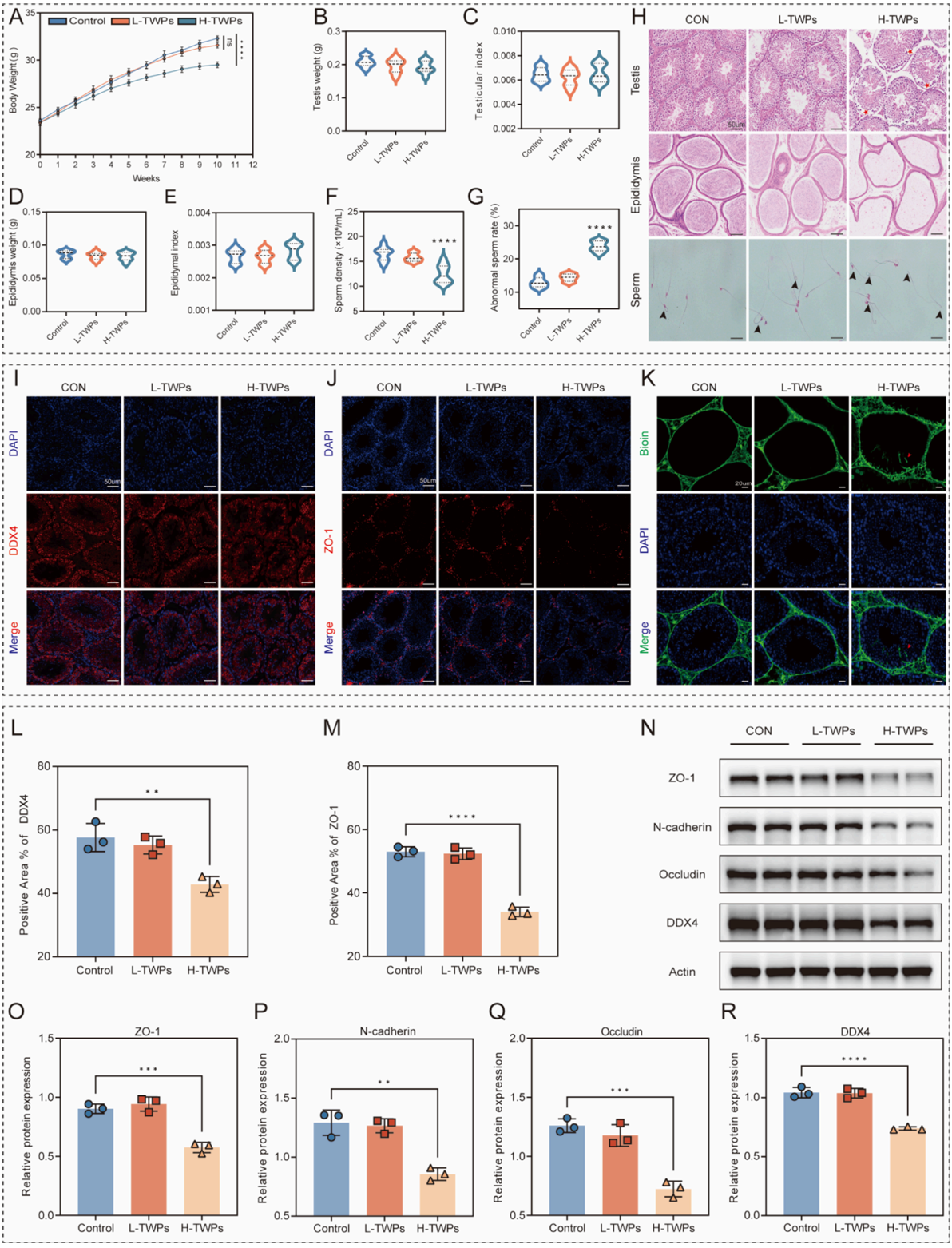


Figure 1

Oral TWPs administration compromises sperm production and BTB function in mice. Male BALB/c mice, 3 weeks of age, were gavaged with ultrapure water, L-TWPs (5 mg kg^{-1} day^{-1}), or H-TWPs (50 mg kg^{-1} day^{-1}) for 70 days. (A) Body-weight change over time. (B,C) Testis weight shown as absolute weight (B) and body weight-normalized index (C). (D,E) Epididymis weight shown as absolute weight (D) and relative index (E). (F) Epididymal sperm density. (G) Percentage of abnormal spermatozoa. For (A-G), n = 8 mice per group. (H) H&E-stained testes and epididymides with representative sperm morphology. Red arrows indicate injured seminiferous tubules; black arrows indicate abnormal spermatozoa. Scale bars: 50 μm. (I,J) Testicular DDX4 (I) and ZO-1 (J) immunofluorescence. Scale bars: 50 μm. (K) Biotin tracer assay for BTB permeability. Biotin, green; DAPI, blue. Red arrows denote biotin extension beyond the basal compartment. Scale bars: 20 μm. (L,M) Quantified DDX4-positive (L) and ZO-1-positive (M) areas. (N) Immunoblots for ZO-1, N-cadherin, occludin, and DDX4. (O-R) Densitometry for ZO-1 (O), N-cadherin (P), occludin (Q), and DDX4 (R). For (L,M,O-R), n = 3 mice per group. Values are mean ± SD. **P < 0.01, ***P < 0.001, and ****P < 0.0001 versus control.

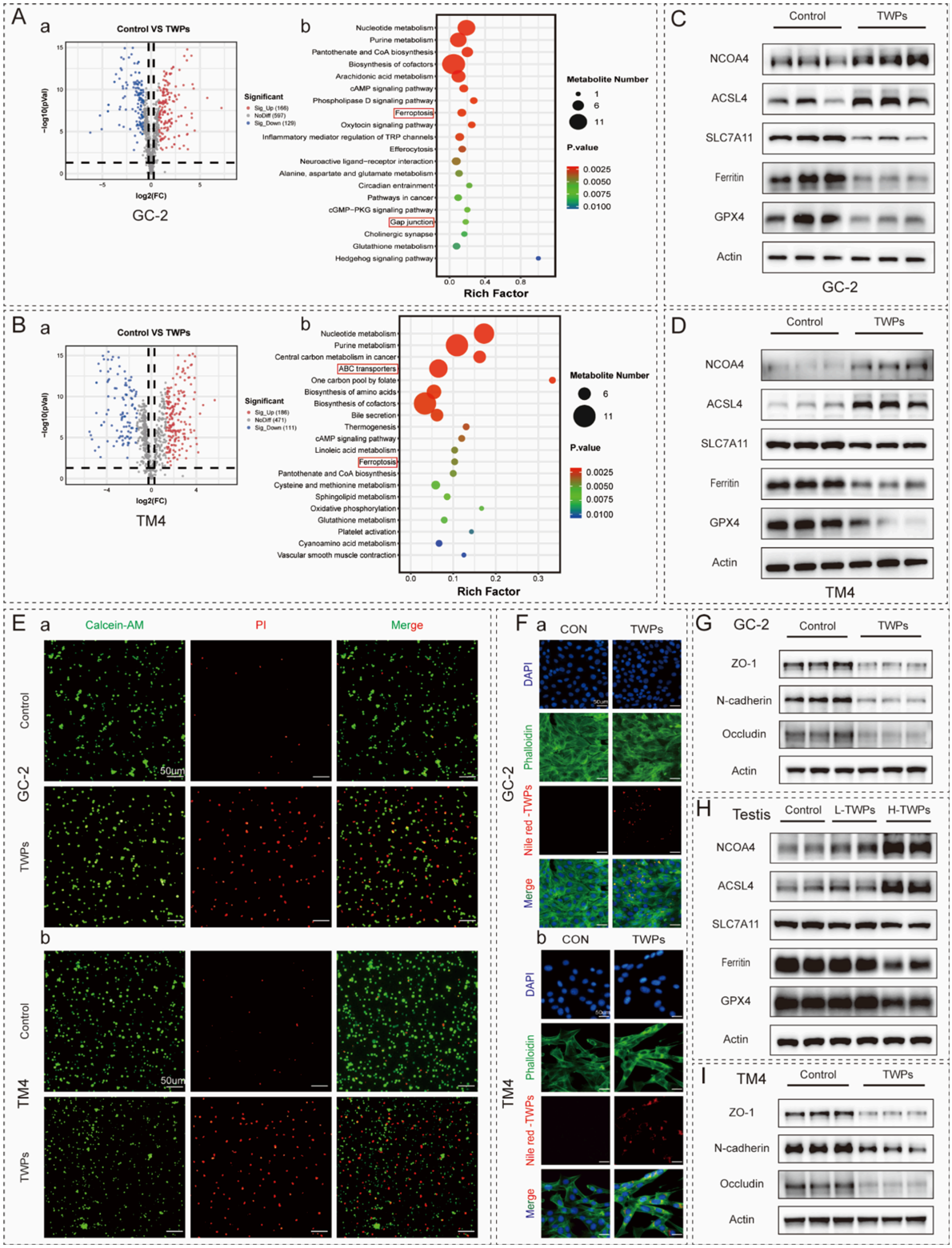


Figure 2

TWPs exposure induces ferroptosis and disrupts junctional integrity in GC-2 and TM4 cells. Cells were incubated with TWPs (400 μg/mL) for 24 h. (A) GC-2 metabolomics: (a) differential-metabolite volcano plot; (b) KEGG pathway enrichment. (B) TM4 metabolomics: (a) differential-metabolite volcano plot; (b) KEGG pathway enrichment. (C,D) Immunoblots for ferroptosis-related proteins in GC-2 (C) and TM4 (D) cells. (E) Calcein-AM/PI live/dead staining in (a) GC-2 and (b) TM4 cells. Viable cells are green; dead

cells are red. Scale bars: 50 μm. (F) F-actin staining and Nile Red-labelled TWPs localization in (a) GC-2 and (b) TM4 cells. Green, F-actin; red, TWPs; blue, DAPI-labelled nuclei. Scale bars: 50 μm. (G,I) Immunoblots for junctional proteins in GC-2 (G) and TM4 (I) cells. (H) Testicular immunoblots for ferroptosis-related proteins.

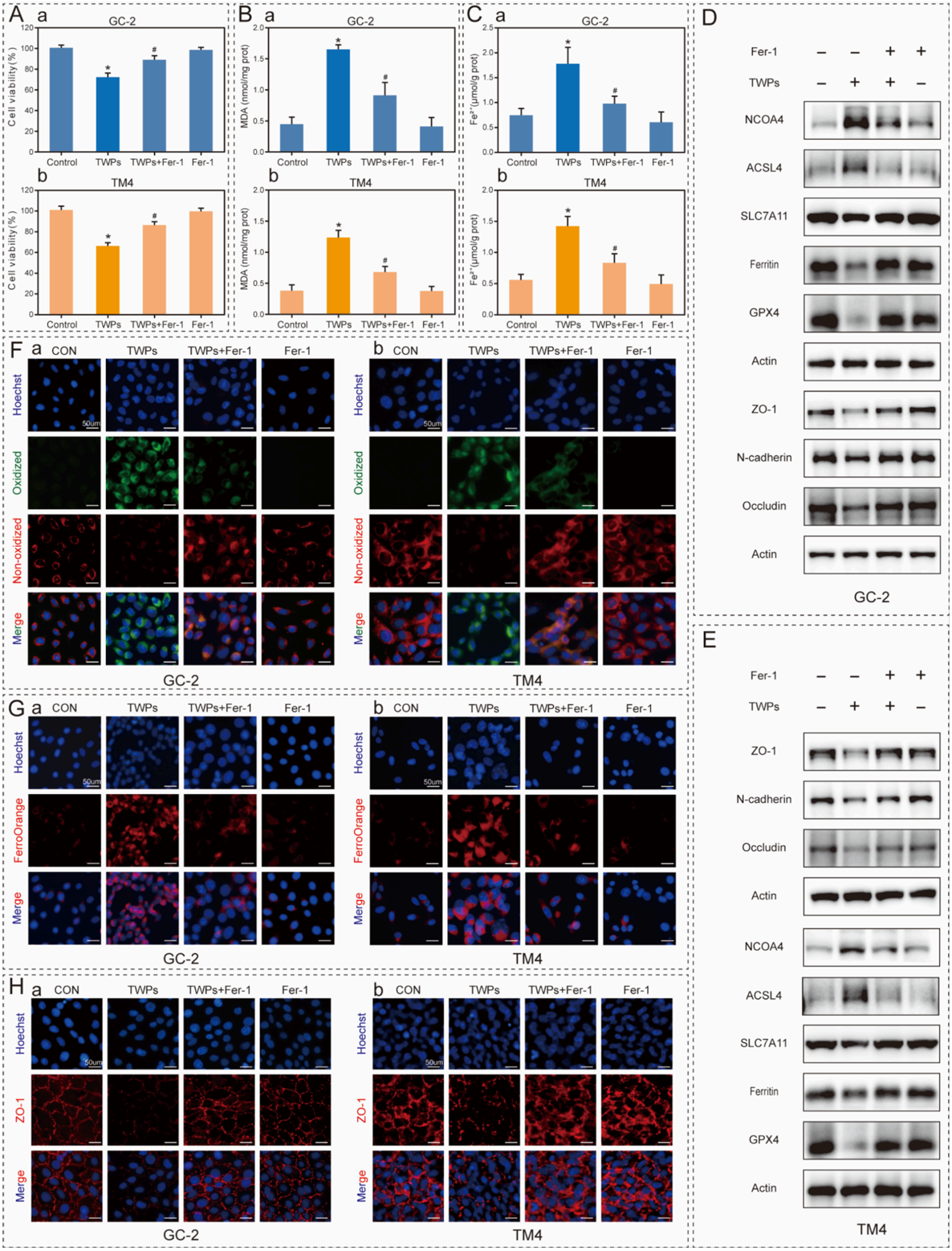


Figure 3

Fer-1 protects GC-2 and TM4 cells from TWPs-induced ferroptotic injury and junctional disruption. (A) CCK-8 viability results for GC-2 (a) and TM4 (b) cells. (B) MDA concentrations in GC-2 (a) and TM4 (b) cells. (C) Labile Fe^{2+} concentrations in GC-2 (a) and TM4 (b) cells. (D,E) Immunoblot detection of ferroptosis- and junction-related proteins in GC-2 (D) and TM4 (E) cells. (F) C11-BODIPY 581/591 imaging of lipid peroxidation in GC-2 (a) and TM4 (b) cells; oxidized probe appears green rather than red. Nuclei are blue (Hoechst). Scale bars: 50 μm. (G) FerroOrange imaging of intracellular Fe^{2+} in GC-2 (a) and TM4 (b) cells. Scale bars: 50 μm. (H) ZO-1 immunofluorescence showing junctional patterning in GC-2 (a) and TM4 (b) cells. Scale bars: 50 μm. Data are mean ± SD from three biological replicates. *$P < 0.05$ versus control; $^{\#}P < 0.05$ versus TWPs.

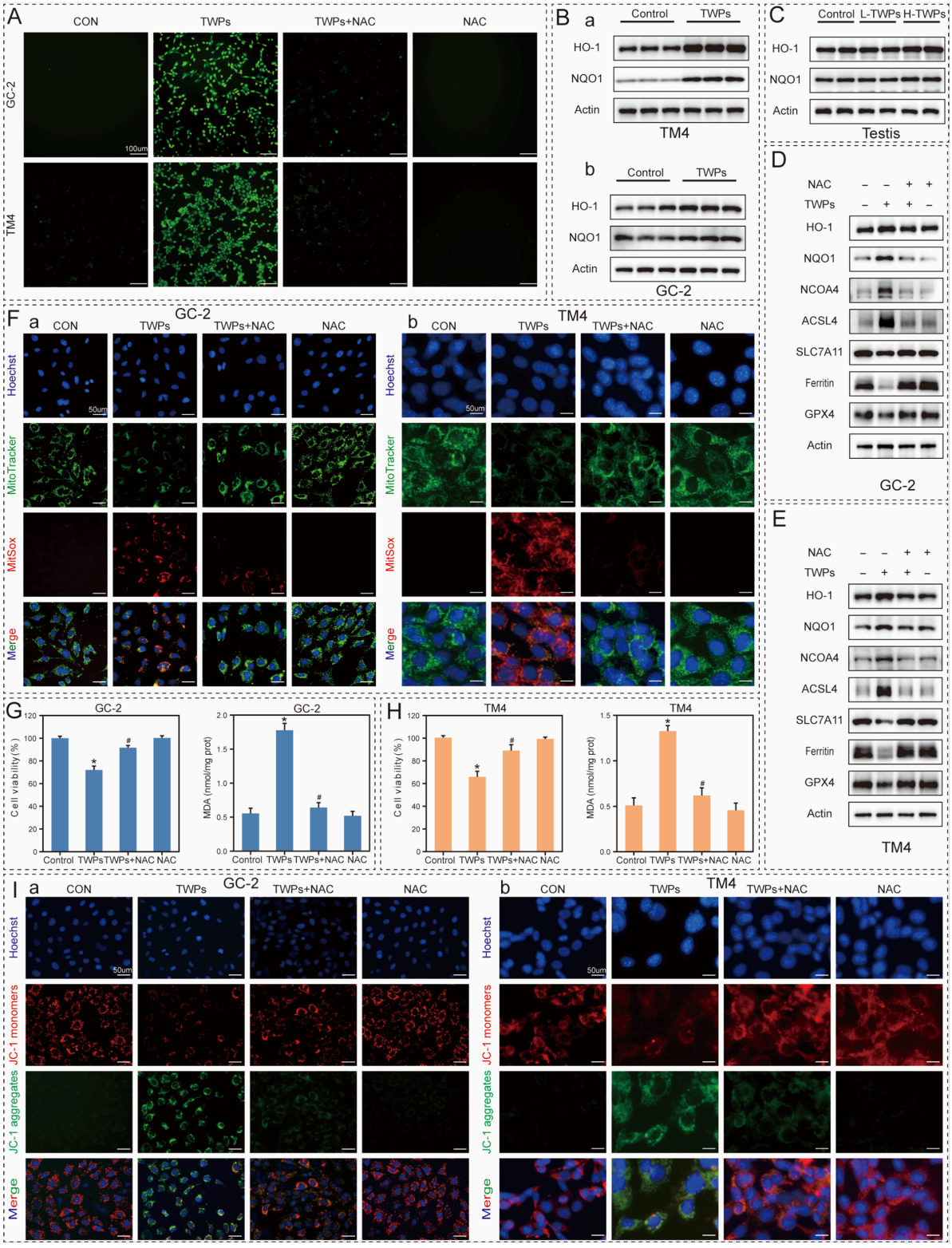


Figure 4

NAC suppresses redox stress, mitochondrial injury, and ferroptosis after TWPs exposure. (A) DCFH-DA fluorescence images of intracellular ROS. Scale bar: 100 μm. (B) HO-1 and NQO1 immunoblots in GC-2 (b) and TM4 (a) cells. (C) Testicular HO-1 and NQO1 immunoblots after the indicated TWPs doses. (D,E) Immunoblot analysis in GC-2 (D) and TM4 (E) cells. (F) MitoTracker/MitoSOX images of mitochondrial architecture and mitochondrial superoxide in GC-2 (a) and TM4 (b) cells. MitoTracker, green; MitoSOX,

red; Hoechst, blue. Scale bar: 50 μm. (G,H) Viability and MDA measurements in GC-2 (G) and TM4 (H) cells. (I) JC-1 imaging of mitochondrial membrane potential in GC-2 (a) and TM4 (b) cells; a higher green/red signal indicates depolarization. Scale bar: 50 μm. Data are mean ± SD from three biological replicates. *P < 0.05 versus control; #P < 0.05 versus TWPs.

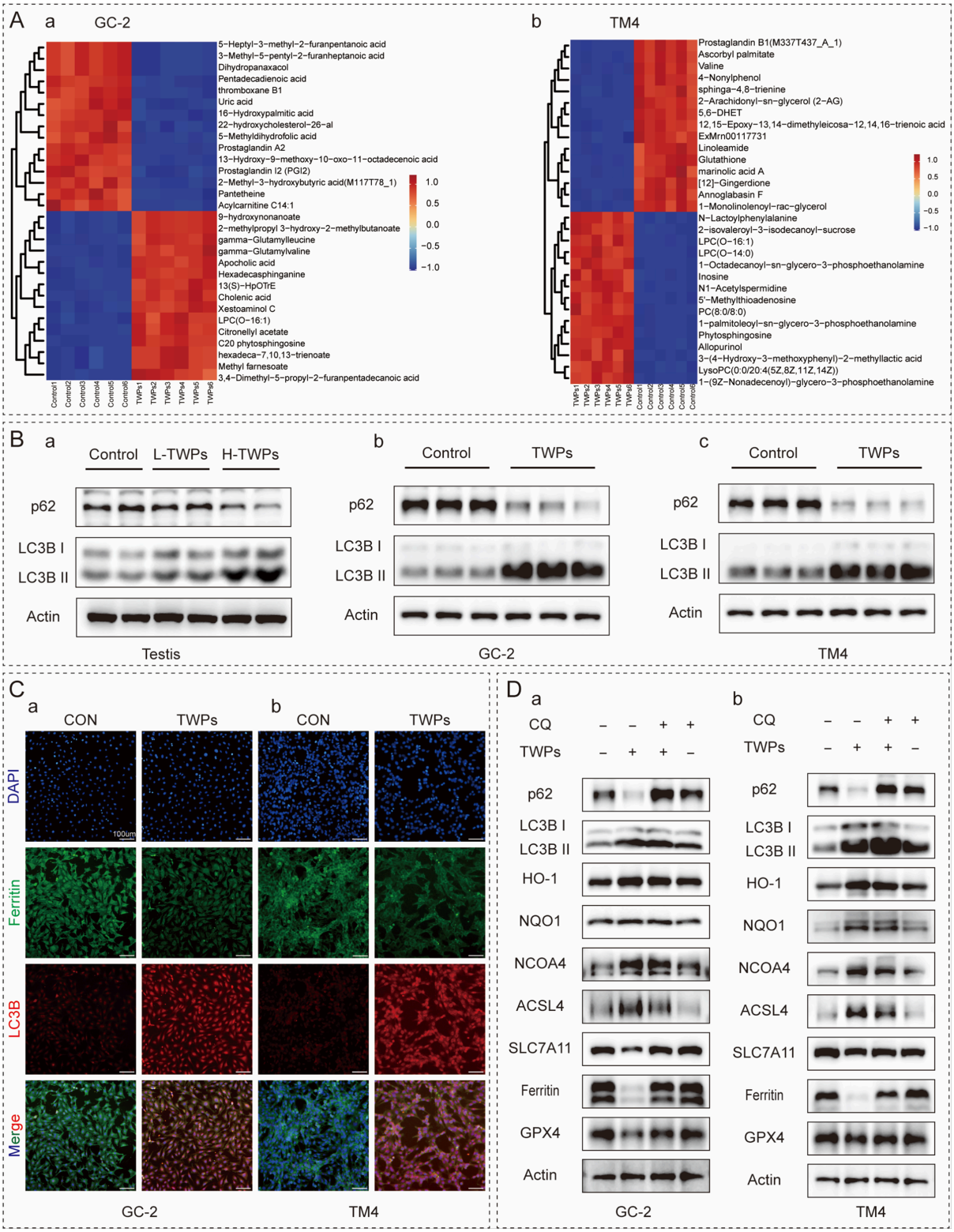


Figure 5

TWPs activate autophagic flux and ferritin degradation in GC-2 and TM4 Cells. (A) Heatmaps clustering metabolites altered by TWPsexposure in GC-2 (a) and TM4 (b) cells. (B) p62 and LC3B immunoblots in testes (a), GC-2 cells (b), and TM4 cells (c). (C) Ferritin-LC3B immunofluorescence in GC-2 (a) and TM4 (b) cells after TWPsexposure. Ferritin, green; LC3B, red; DAPI, blue. Scale bar: 100 μm. (D) Immunoblot analysis of the indicated proteins in GC-2 (a) and TM4 (b) cells treated with CQ.

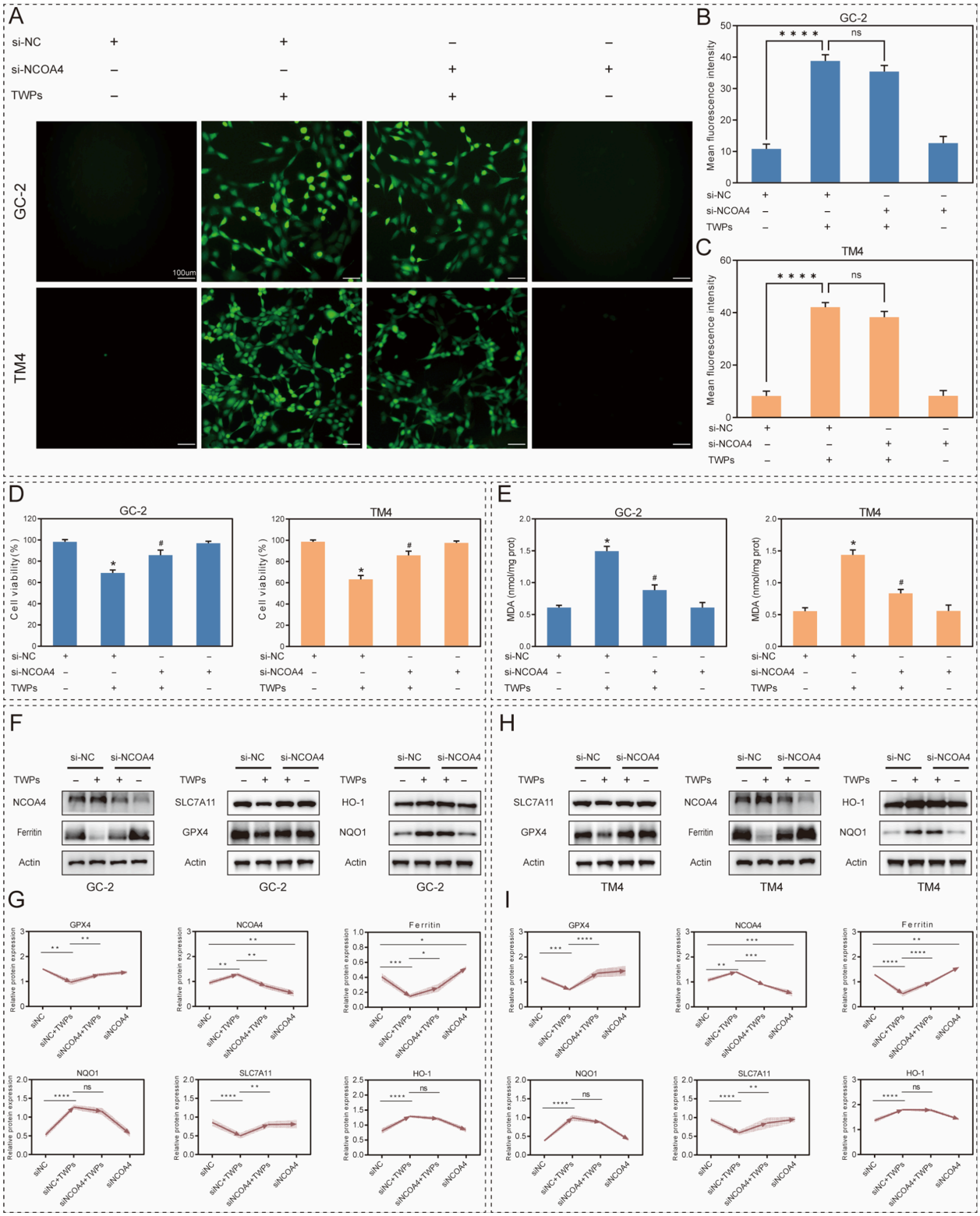


Figure 6

NCOA4 Links TWPs-Induced Oxidative Stress to Ferritinophagy-Driven Ferroptotic Injury. (A) DCFH-DA images showing ROS in GC-2 and TM4 cells after si-NC or si-NCOA4 transfection followed by TWPs exposure. (B,C) Mean DCFH-DA fluorescence intensity in GC-2 and TM4 cells. (D) CCK-8 viability after NCOA4 knockdown and TWPs treatment. (E) MDA levels in GC-2 and TM4 cells under the same conditions. (F,H) Immunoblots for NCOA4, ferritin, SLC7A11, GPX4, HO-1, and NQO1 in GC-2 and TM4 cells. (G,I) Quantification of the indicated bands. Data are mean ± SD from three independent experiments. *P < 0.05 versus si-NC; $^{\#}$P < 0.05 versus si-NC+TWPs. **P < 0.01, ***P < 0.001, ****P < 0.0001, and ns, not significant.

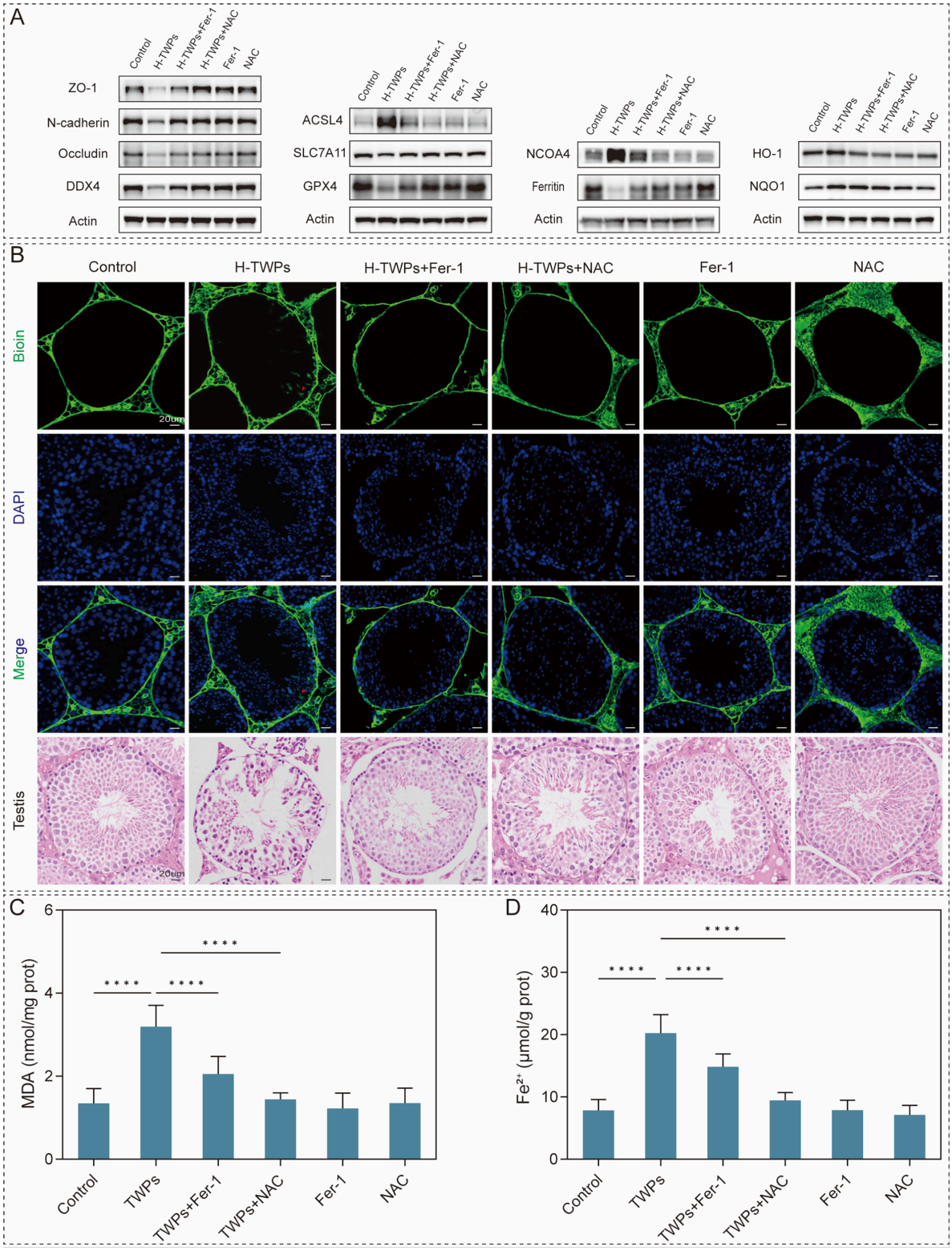


Figure 7

Fer-1 and NAC alleviate TWPs-induced testicular injury in vivo. (A) Immunoblots of the indicated testicular proteins. (B) Biotin tracer and H&E images used to evaluate BTB permeability and testicular histology. Biotin, green; DAPI, blue. Red arrows indicate biotin signal beyond the basal compartment. Scale bars: 20 μm. (C) Testicular MDA. (D) Testicular Fe^{2+}. Data are mean ± SD (n = 8 mice per group).

Supplementary Files

This is a list of supplementary files associated with this preprint. Click to download.

- SupportingInformationinfo.docx
- SupportingInformation.docx
- image2.png